Journal of Advanced Ceramics
先进陶瓷
ISSN 2226-4108
CN 10-1154/TQ
清华大学出版社 Tsinghua University Press
SciOpen

J Adv Ceram 2026, **15**: 9221407

https://doi.org/10.26599/JAC.2026.9221407

Research Article

Dielectric gene engineering in subwavelength-structured amorphous silicon oxycarbide ceramic aerogels for programmable electromagnetic wave absorption

Yong Kong[1,*], Xiaoqian Zhang[1], Jing Wei[1], Yihang Yang[2], Xiaodong Shen[1], Gaofeng Shao[2,*]

[1] *College of Materials Science and Engineering, Jiangsu Collaborative Innovation Center for Advanced Inorganic Function Composites, State Key Laboratory of Materials-Oriented Chemical Engineering, Nanjing Tech University, Nanjing 211816, China*

[2] *School of Chemistry and Materials Science, Jiangsu Key Laboratory of New Energy Devices and Interface Science, Nanjing University of Information Science & Technology, Nanjing 210044, China.*

* Corresponding author.

E-mail: Y. Kong, ykong@njtech.edu.cn;

G. Shao, gfshao@nuist.edu.cn

Just Accepted

Received: September 26, 2026; Revised: October 28, 2026; Accepted: November 11, 2026

©The Author(s) 2026

Abstract: Amorphous ceramics, distinctively represented by silicon oxycarbide (SiOC), are promising electromagnetic wave absorbers owing to their low density and high-temperature stability. To enable programmable attenuation, we propose a dielectric gene engineering strategy, fabricating subwavelength-structured amorphous SiOC aerogels via wet spinning, sol-gel processing, supercritical drying, and subsequent thermal treatments. At the macroscopic level, the customized multi-scale void network optimizes impedance matching, enhances multiple scattering and reflections, and effectively prolongs the propagation path of electromagnetic waves. At the microscale, intrinsic dielectric genes including the conductive sp^2 carbon phase, dielectric SiC nanocrystals, asymmetric SiO_xC_{4-x} tetrahedra, and the interfaces of these heterogeneous nanodomains are established by manipulating carbothermal reduction and post-oxidation thermal etching. This engineered structural evolution achieves an optimal synergy among conduction loss from the carbon network, interfacial polarization at heterogeneous boundaries, and dipolar polarization induced by the asymmetric tetrahedra. Consequently, driven by this macro-micro synergy, these amorphous ceramic aerogels achieve programmable and frequency-tunable absorption spanning the C, X, and Ku bands. They deliver minimum reflection losses of –57.87 dB at 5.36 GHz, –70.09 dB at 9.04 GHz, and –54.06 dB at 14.28 GHz. This work demonstrates that integrating subwavelength architectures with dielectric gene engineering provides a paradigm for designing lightweight and frequency-programmable ceramic absorbers.

Keywords: SiOC ceramic; electromagnetic wave absorbers; aerogel microspheres; frequency tunable; dielectric gene.

Just Accepted

1 Introduction

The escalating crisis of electromagnetic pollution demands electromagnetic wave absorbers (EWA) that are lightweight, broadband, and environmentally resilient[1-3]. Current materials fundamentally fail

to meet these stringent criteria: magnetic absorbers are high density and poor corrosion resistance, whereas conductive carbon networks suffer from severe impedance mismatch and limited high-temperature resistance. Overcoming these bottlenecks requires shifting focus towards lightweight, thermally stable, and dielectric-tunable ceramic absorbers[4-7].

Polymer-derived ceramics, especially silicon oxycarbide (SiOC), have attracted considerable attention as promising EWA because of their low density, thermal stability, oxidation resistance, and adjustable dielectric properties[8-10]. The unique amorphous SiOC network and free carbon phase in SiOC provide abundant dipolar polarization centers, interfacial polarization sites, and conduction loss pathways[11-13]. Moreover, the microstructure and phase composition of SiOC can be effectively tailored by controlling the precursor chemistry and pyrolysis conditions[14, 15]. During high-temperature treatment, carbothermal reduction can induce the formation of SiC nanocrystals and promote the structural evolution of free carbon, thereby generating heterogeneous interfaces and enhancing dielectric loss[16, 17]. These features make SiOC an ideal platform for designing high-performance dielectric electromagnetic absorbers[18, 19]. Despite these advantages, realizing frequency-tunable absorption across different bands remains challenging because the relationship between microstructural evolution and dielectric response has not been sufficiently clarified[3].

Recently, the concept of regulating the intrinsic dielectric response through microstructural design has emerged as a promising paradigm for the development of electromagnetic absorbers[20]. This dielectric response is fundamentally dictated by several key dielectric genes, including conduction loss, interfacial polarization, dipolar polarization, and impedance matching[20-22]. In SiOC ceramics, these inherent genes are intimately tied to the distribution, composition, and synergistic interaction of nanoscale domains, including free carbon, SiC nanocrystals, the amorphous SiOC matrix, and secondary dielectric or magnetic phases[9, 23-26]. Consequently, hetero-nanodomain engineering represents a powerful strategy for modulating the dielectric genes in SiOC-based absorbers[9, 27, 28]. By rationally tailoring these nanoscale heterogeneous domains, it becomes possible to precisely control

Just Accepted

electron transport, polarization relaxation, and electromagnetic energy dissipation, thereby unlocking highly tunable absorption behavior.

In addition to compositional and structural regulation, the macroscopic architecture of absorbers also plays a crucial role in electromagnetic wave absorption[8, 10, 29, 30]. Aerogel microspheres possess low density, high porosity, large specific surface area, and multiple scattering pathways, which are favorable for lightweight absorption and enhanced electromagnetic attenuation[31, 32]. Compared with bulk monoliths or powders[33-36], aerogel microspheres offer improved processability, structural controllability, and potential compatibility with coating or composite systems[29, 37]. Combining the porous aerogel microsphere architecture with the intrinsic dielectric tunability of SiOC ceramics is therefore a promising approach for constructing lightweight and frequency-selective electromagnetic absorbers.

Herein, SiOC aerogel microspheres (SiOCAMs) were fabricated by wet spinning combined with sol–gel processing, supercritical drying, and high-temperature thermal treatment. A dielectric gene regulation strategy based on hetero-nanodomain engineering was proposed to achieve frequency-tunable electromagnetic wave absorption. By adjusting the carbothermal reduction temperature, hetero-nanodomains composed of free carbon, SiC nanocrystals, and an amorphous SiOC matrix were progressively constructed. Furthermore, post-oxidation thermal etching was employed to selectively tailor the free carbon phase, thereby optimizing conduction loss, polarization relaxation, and impedance matching. The engineered hetero-nanodomains effectively modulate key dielectric genes, including conduction loss from free carbon, interfacial polarization at free carbon, SiC and SiOC interfaces, and dipolar polarization associated with defects and asymmetric SiO_xC_{4-x} tetrahedra. As a result, frequency-tunable electromagnetic wave absorption across the C, X, and Ku bands was achieved. This work provides a feasible strategy for designing lightweight, thermally stable, and programmable ceramic-based electromagnetic wave absorbers.

Just Accepted

2 Experimental

2.1 Materials

Resorcinol (R), ethanol (EtOH, 99.7%), formaldehyde (F, 37 wt%), and 3-aminopropyltriethoxysilane (APTES) were obtained from China National Pharmaceutical Group Chemical Reagent Co., Ltd., Wuxi Yasheng Chemical Co., Ltd., along with Aladdin Biochemical Technology Co., Ltd. and Xilong Science Co., Ltd., respectively. The reagents were used as received without further purification.

2.2 Synthesis of SiOCAMs

SiOCAMs were prepared via carbothermal reduction of RF/SiO_2 hybrid aerogel microspheres. In a typical synthesis of RF/SiO_2 hybrid aerogel microspheres, 2.75 g of resorcinol was first dissolved in 3.75 mL of aqueous formaldehyde under continuous stirring to obtain a homogeneous solution. Subsequently, 20 mL of ethanol was added, and the mixture was stirred for 20 min. Then, 11.75 mL of APTES was introduced dropwise under stirring, followed by an additional stirring period of 30 min. The resulting precursor solution was then dropped into dimethyl silicone oil maintained at 90 °C, leading to the formation of wet gel microspheres with diameters of approximately 2 mm. Gelation occurred within 5 min, and the obtained microspheres were further aged in the oil bath for 12 h to make sure the crosslinking between resorcinol and formaldehyde proceeds adequately to improve the robustness of the microspheres.

After aging, the wet gel microspheres were immersed in ethanol for solvent exchange at room temperature for 3 d, with the ethanol refreshed every 12 h. The RF/SiO_2 hybrid aerogel microspheres were finally obtained after supercritical CO_2 drying, and the drying time was 4 h at 10 MPa and 50 °C. Carbothermal reduction of the RF/SiO_2 hybrid aerogel microspheres was carried out in a tubular furnace under an argon flow of 200 mL min^{-1} at a heating rate of 2 °C min^{-1}. The samples were heated to terminal temperatures of 1200, 1300, 1400, and 1500 °C and held for 1 h. The corresponding products were denoted as SiOC1200, SiOC1300, SiOC1400, and SiOC1500, respectively. To further tailor the free-carbon content and skeletal architecture, the SiOC samples (SiOC1200–1500) were

Just Accepted

calcined in air at 600 °C for 2 h in a muffle furnace. The resulting samples were denoted as SiOC1200-TE, SiOC1300-TE, SiOC1400-TE, and SiOC1500-TE, respectively. Notably, SiOC1200-TE was excluded from subsequent characterization due to structural cracking.

2.3 Characterization

The phase structure of SiOC aerogel microspheres were characterized with X-ray diffraction (XRD, X'Pert Pro, Panalytical, Netherlands). Raman spectra were obtained using a Renishaw in Via Raman microscope at an excitation wavelength of 532 nm. X-ray photoelectron spectroscopy (XPS, Thermo Fisher Scientifc, USA) was employed with a monochromatic Al Kα X-ray source to analyze the chemical bonding status. N_2 adsorption/desorption isotherms were determined by an N_2 adsorption analyzer (Belsorp miniX, MicrotracBEL, Japan). Specific surface area and pore size distribution of SiOC aerogel microspheres were determined using Brunauer-Emmett-Teller (BET), and Barrett-Joyner-Halenda (BJH) methods, respectively. The microstructure of SiOCAMs were examined with scanning electron microscope (SEM, JEOL JSM-7600F, Japan). The phase structure were determined with transmission electron microscope (TEM, TF-G20, Thermo Fisher Scientific, USA). Electromagnetic parameters of SiOCAMs were measured with a vector network analyzer (N5234B PNA-X, Agilent) with a frequency range of 2–18 GHz. The test samples were prepared by immersing SiOCAMs with paraffin and compacted into toroidal with outer diameter of 7.00 mm and inner diameter of 3.04 mm.

2.4 Radar cross-section (RCS) simulation

The radar cross-section of SiOCAMs were simulated using CST Studio Suite 2025. The model consisted of a 200×200 mm^2 square structure comprising a top absorbing layer and a bottom perfect electric conductor (PEC) layer. The thickness of the bottom PEC layer was set to 1 mm. Open boundary conditions were applied in all directions, and the scattering directions were defined using the theta and phi angles in a spherical coordinate system. The RCS vaules can be described as follows:

$$\sigma(dB\ sm) = 10\log((4\pi S/\lambda^2)\,|\,E_s/E_i\,|)^2 \qquad \text{(Eq.1)}$$

Just Accepted

where S denotes the area of the target simulation model; λ is the wavelength of EM wave, and E_s and E_i represent the electric field intensity of the scattered wave and incident wave, respectively.

2.5 Electromagnetic Simulation

To investigate the internal electromagnetic attenuation mechanisms, numerical simulations were carried out using CST Studio Suite 2025[38, 39]. The geometric model was constructed as a 3×3×3 tightly packed spherical array with a uniform sphere radius of 0.90 mm and 0.78 mm for SiOC1200 and SiOC1400-TE, respectively. Open boundary conditions were applied in all directions, and the model was excited by a linearly polarized incident plane wave. To elucidate the microwave absorption origins, 3D field monitors were set up to record the distributions of the electric field, current density, and volumetric power loss on the structural surfaces at representative frequencies of 5 GHz, 10 GHz, and 15 GHz.

3 Results and discussion

3.1 Fabrication and structure of SiOCAMs

The synthesis process for the SiOCAMs, involving a wet spinning, sol-gel followed by supercritical CO_2 drying, carbothermal reduction, and thermal etching, is schematically illustrated in Fig. 1a. The formation and structural integrity of the gel microspheres are governed by the temperature dependency of the sol–gel polymerization and molecular hybridization. Initially, sol preparation is conducted at room temperature to inhibit the polycondensation between resorcinol and formaldehyde, keeping the sol in a low-viscosity, homogeneous liquid state to prevent premature clogging. When introduced into the silicone oil bath at 90 °C, the thermal activation triggers rapid polycondensation, achieving a swift sol-to-gel transition within 5 min. Simultaneously, the interfacial tension and the slightly higher density of the hybrid sol relative to the silicone oil prevent droplet deformation and aggregation, ensuring a high degree of sphericity. Throughout this process, APTES serves as a silane coupling agent that covalently bridges the phenolic resols and silica networks at the molecular scale via nucleophilic addition and co-condensation. Consequently, a chemically crosslinked RF/SiO_2 interpenetrating

Just Accepted

network is formed, comprehensively improving structural homogeneity and integrity to resist capillary forces and high-temperature carbothermal reduction without structural collapse. As revealed by the macroscopic optical photographs (Fig. 1b), the microspheres maintain structural integrity, exhibiting no visible cracks or fragmentation after undergoing carbothermal reduction and subsequent thermal etching. However, the processing temperature influences the macroscopic dimensions. As depicted in Fig. 1c, elevating the carbothermal reduction temperature from 1200 °C to 1500 °C induces a volumetric contraction, resulting in a distinct decrease in the microsphere diameter from 1.80 mm to 1.32 mm. This shrinkage is driven by the carbothermal reduction reactions at higher temperatures, which promotes mass consumption and structural densification.

Microstructurally, the SiOC microspheres exhibit a well-defined hierarchical architecture. SEM images reveal that the outer surface is characterized by a relatively dense assembly of sintered nanoparticles (Fig. 1d and Fig. S1), whereas the interior preserves a highly interconnected, three-dimensional porous network composed of nanoparticle skeletons and nanopores (Fig. 1e and Fig. S1). Further observations indicate that higher reduction temperatures aggravate nanoparticle sintering (Fig. S1), causing a progressive loss of structural porosity on both the surface and within the internal network. Following the thermal etching process, the overall surface morphology remains largely invariant; nevertheless, the internal porosity experiences a noticeable resurgence (Fig. S2).

To understand the evolution of the specific porous architecture and its correlation with processing conditions, specific surface area (SSA) and pore structure were characterized using N_2 adsorption–desorption measurements. Fig. S3a illustrates that all investigated samples exhibit representative Type IV isotherms with distinct hysteresis loops. This is further corroborated by the corresponding pore size distribution curves (Fig. S3b), where the pore diameters are predominantly concentrated in the mesoscale range (10–20 nm). A detailed quantitative analysis, summarized in Table S1, reveals a dramatic structural evolution governed by both the carbothermal reduction temperature and the subsequent thermal etching process. Initially, as the processing temperature increased from 1200 °C

Just Accepted

to 1500 °C, the pristine aerogel underwent high-temperature sintering and densification. Consequently, the SSA decreased from 162.87 $m^2 g^{-1}$ (SiOC1200) to merely 25.78 $m^2 g^{-1}$ (SiOC1500), accompanied by a pore volume collapse and a density surge up to 1.185 g cm^{-3}.

Crucially, the post-oxidation thermal etching serves as an effective pore-reconstruction strategy. By selectively consuming internal free carbon domains, copious new mesopores were generated, rescuing the collapsed networks of the high-temperature samples. Compared to their unetched counterparts, the etched samples exhibit a recovery in porosity. Taking the 1500 °C group as a prime example, thermal etching boosted the SSA from 25.78 $m^2 g^{-1}$ to 456.71 $m^2 g^{-1}$ (SiOC1500-TE), and suppressed the density back down to 0.752 g cm^{-3}. This is attributed to the selective oxidation of free carbon at 600 °C, which unblocks closed pores and creates new pore structures. Concurrently, the oxidation resistance of the SiC/SiOC skeleton maintains structural integrity, leading to an increase in SSA and a decrease in density. This abundant introduction of air-filled mesopores not only guarantees the lightweight requirement for practical implementation but also profoundly lowers the effective permittivity of the materials, establishing a highly favorable architectural foundation for optimizing electromagnetic impedance matching.

Just Accepted

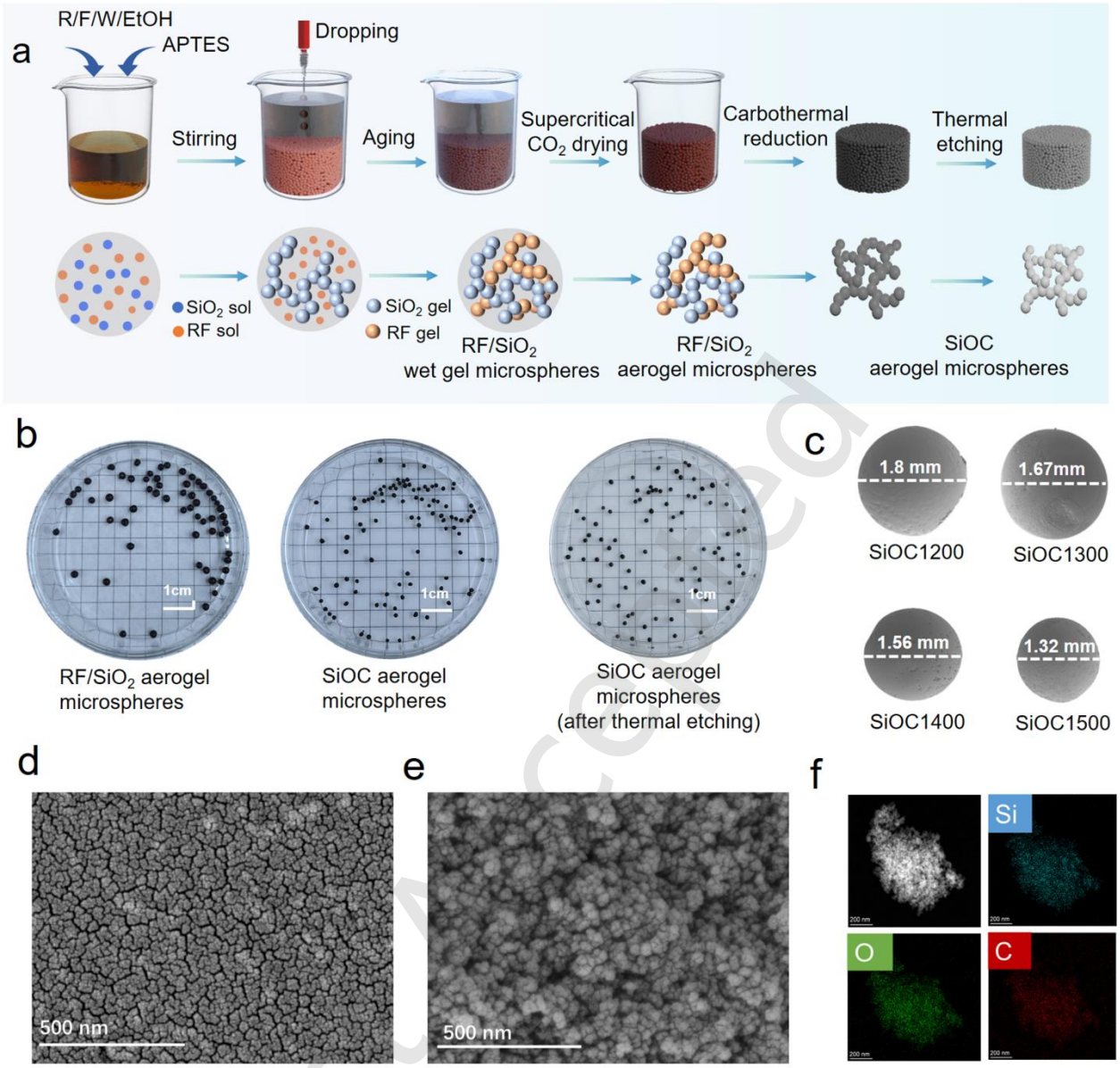


Fig. 1 (a) Schematic showing the preparation route of the SiOC aerogel microspheres. (b) Optical photographs of the RF/SiO_2, unetched SiOC, and thermally etched SiOC aerogel microspheres. (c) SEM images displaying the diameters and shrinkage of the SiOC microspheres carbonized at different temperatures. (d) Surface and (e) inner SEM images of SiOC1200 aerogel microspheres. (f) Dark-field TEM image and EDS elemental mapping images confirming the uniform distribution of Si, O, and C atoms within the sample.

Furthermore, elemental mapping confirms a highly uniform spatial distribution of Si, O, and C within the aerogel microspheres (Fig. 1f and Fig. S4). This intrinsic chemical homogeneity provides a reliable structural basis for the subsequent thermal etching step, ensuring stable reconfiguration of the carbon nanodomain connectivity. Notably, the etched samples (SiOC1300-TE, SiOC1400-TE, and SiOC1500-TE) inherit this pristine elemental uniformity (Fig. S5), while the overall stoichiometric

evolution is dynamically governed by the competitive extents of structural carbonization and carbothermal reduction reactions (Table S2).

3.2 Phase composition and chemical structure of SiOCAMs

The phase composition and chemical evolution of the SiOCAMs during carbothermal reduction, alongside the structural reconfiguration induced by the subsequent thermal etching process, were systematically investigated. As depicted in the XRD patterns (Fig. 2a), the unetched microspheres undergo a highly temperature-dependent phase transformation. Lower-temperature treatments (below 1400 °C) yield broad diffraction peak, indicating the retention of an amorphous SiOC glass network. Conversely, at elevated temperatures (1500 °C), distinct diffraction peaks assigned to cubic silicon carbide (SiC, JCPDS No. 29-1129)[40]. This sharp transition verifies the onset of a vigorous carbothermal reduction reaction, triggering the *in-situ* crystallization of SiC nanodomains. After thermal etching, the XRD patterns of both SiOC1300-TE and SiOC1400-TE are dominated by a broad diffraction peak, and distinct reflections are assigned to crystallites of SiC in SiOC1500-TE (Fig. S6). Further structural insights into the intrinsic free carbon phase were elucidated via Raman spectroscopy (Fig. 2b–d). All spectra exhibit the characteristic defect-induced D band (~1350 cm^{-1}) and the in-plane graphitic G band (~1580 cm^{-1}), which can be deconvoluted into four discrete vibrational modes (T, D, D" and G). For the unetched series, the intensity ratio of the D to G bands (I_D/I_G) steadily declines from 2.185 (SiOC1200) to 1.908 (SiOC1500). This continuous reduction quantitatively signifies the healing of structural defects and an enhanced degree of graphitization within the free carbon network at higher temperatures. Following the carbon etching process (Fig. 2d), the I_D/I_G values experience a further decline from 1.908 to 1.806 for the 1500 °C sample. This monotonic trend implies the selective oxidative removal of highly defective carbon borders and amorphous carbon species, leaving behind a more highly ordered, graphitic carbon framework.

High-resolution XPS was employed to monitor the transformation of skeletal chemical bonding states. The C 1s and Si 2p core-level spectra of the unetched samples directly corroborate the thermally driven

Just Accepted

phase transition (Fig. 2e and f). Concomitant with the increasing reduction temperature, particularly beyond 1400 °C, the relative intensities of the C–Si peak in the C 1s spectra and the corresponding Si–C peak (~101.5 eV) in the Si 2p spectra exhibit a dramatic augmentation. This provides compelling spectroscopic evidence for the substantial consumption of initial Si–O bonds to construct bridging Si–C networks. After the oxidation-based carbon etching post-treatment (Fig. 3g and 3h), the fundamental Si–C and Si–O structural frameworks are preserved. Meanwhile, the relative intensities of oxygenated carbon species (C–O, C=O) subtly augment, which is a reasonable consequence of the oxidation during the selective carbon burn-off process.

Ultimately, the elemental trajectory of these microspheres is elegantly mapped within a Si–O–C ternary phase diagram (Fig. 2i). For the unetched series, increasing the carbothermal reaction temperature straightforwardly drives the composition toward the carbon- and silicon-rich boundaries. This elemental migration is dynamically governed by the massive depletion of internal oxygen. Conversely, the etched samples demonstrate a striking compositional reversal, migrating sharply backward toward the oxygen–silicon axis. This shift affords definitive proof of the successful partial elimination of the free carbon phase, ultimately validating the structural feasibility of elemental rebalancing via selective thermal oxidation.

Just Accepted

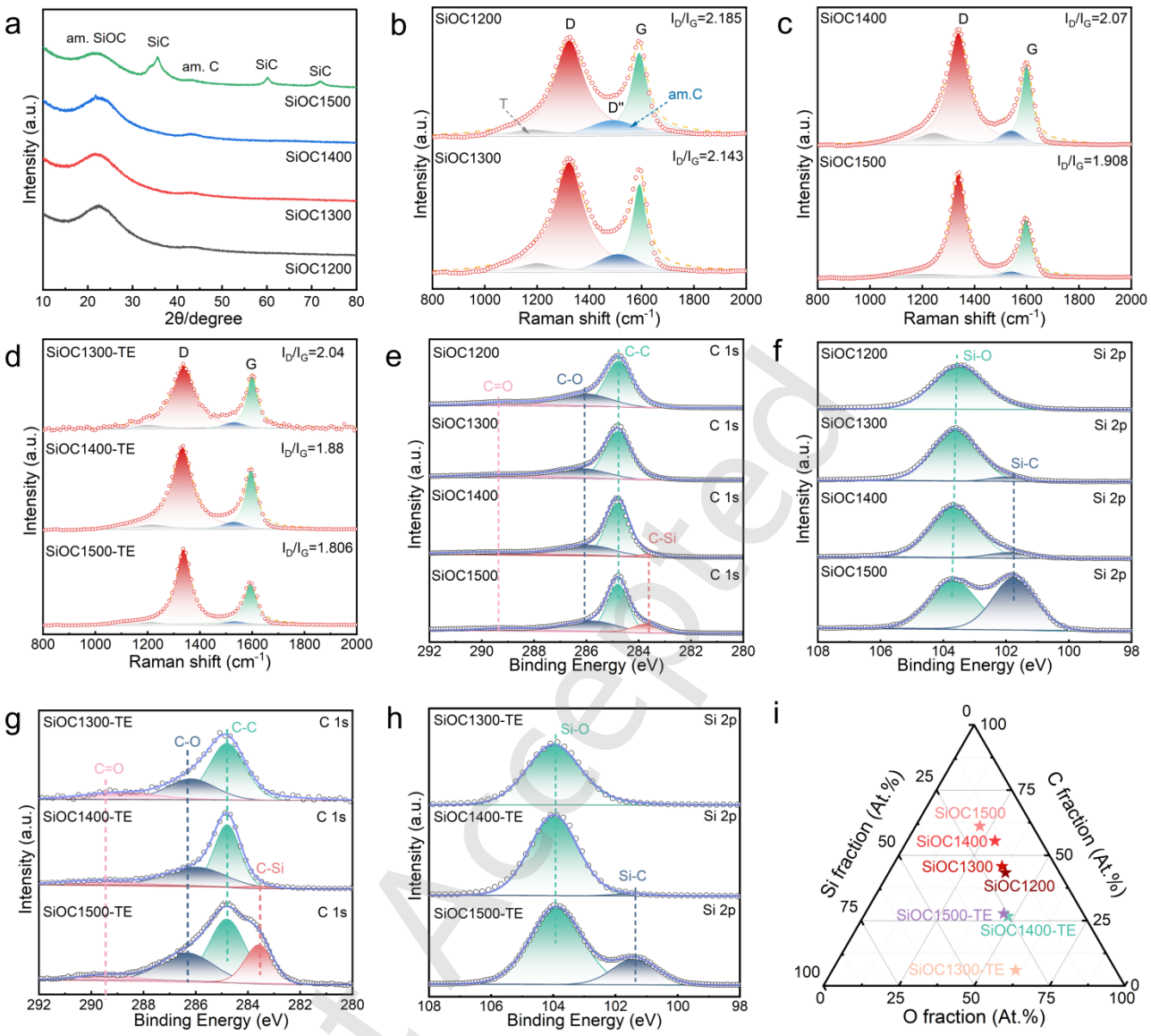


Fig. 2 (a) XRD patterns of the pre-etched SiOC aerogel microspheres at different temperatures. Deconvoluted Raman spectra of (b, c) the unetched samples and (d) samples after thermal etching. (e, f) High-resolution XPS C 1s and Si 2p spectra of the unetched SiOC samples. (g, h) High-resolution XPS C 1s and Si 2p spectra of the thermally etched samples. (i) Ternary atomic diagram illustrating the proportional changes of Si, O, and C elements across the diverse samples before and after the etching processing.

Just Accepted

3.3 Microstructure of SiOCAMs

To gain an atomic-level perspective on the structural evolution and the genesis of hetero-nanodomains, high-resolution transmission electron microscopy (HRTEM) was conducted. For the unetched samples (Figures 3a–c), a distinct progression in structural ordering is visualized. The SiOC1200 sample exhibits an amorphous structure (Fig. S7). In the SiOC1300 and SiOC1400 samples, the matrix is

predominantly populated by aggregated free carbon nanodomains (Fig. 3a,b). Their corresponding magnified images reveal recognizable multi-layer turbostratic carbon structures with an interlayer d-spacing of ~0.346–0.348 nm, which is characteristic of the graphitic (002) plane (Fig. $3a_1$ and $3b_1$). A striking nanostructural transition occurs at 1500 °C (Fig. 3c). Alongside the highly ordered graphitic carbon regions (Fig. $3c_1$), a new crystalline phase emerges (Fig. $3c_2$). The measured lattice fringe of 0.25 nm matches the (111) crystallographic plane of SiC. This direct observation confirms that elevated temperatures not only promote the graphitization of free carbon but also trigger the *in-situ* carbothermal reduction to precipitate highly crystalline SiC nanodomains, forming a C–SiC dual-phase system within the SiOC amorphous matrix.

Following the thermal etching process, the microstructural networks of the composites undergo a reconfiguration (Fig. 3d–f). The HRTEM images of SiOC1300-TE and SiOC1400-TE elucidate that while fragments of the graphitic layers are retained (Fig. $3e_1$), the previously continuous carbon frameworks have been partially disrupted by the oxidative etching, leaving behind more localized, tortuous, or defect-rich carbon distinct domains (Fig. $3d_1$). Most importantly, for the SiOC1500-TE sample (Fig. 3f), the SiC nanocrystals intricately coexist with the residual well-graphitized carbon domains (Fig. $3f_1$-f_2). This post-etching structural preservation definitively proves that the etching process selectively trims the over-percolated amorphous/defective carbon networks while sustaining the essential crystalline SiC and ordered carbon. This selective network breakage is crucial for mitigating purely continuous conductive paths, thereby preventing severe impedance mismatch.

Just Accepted

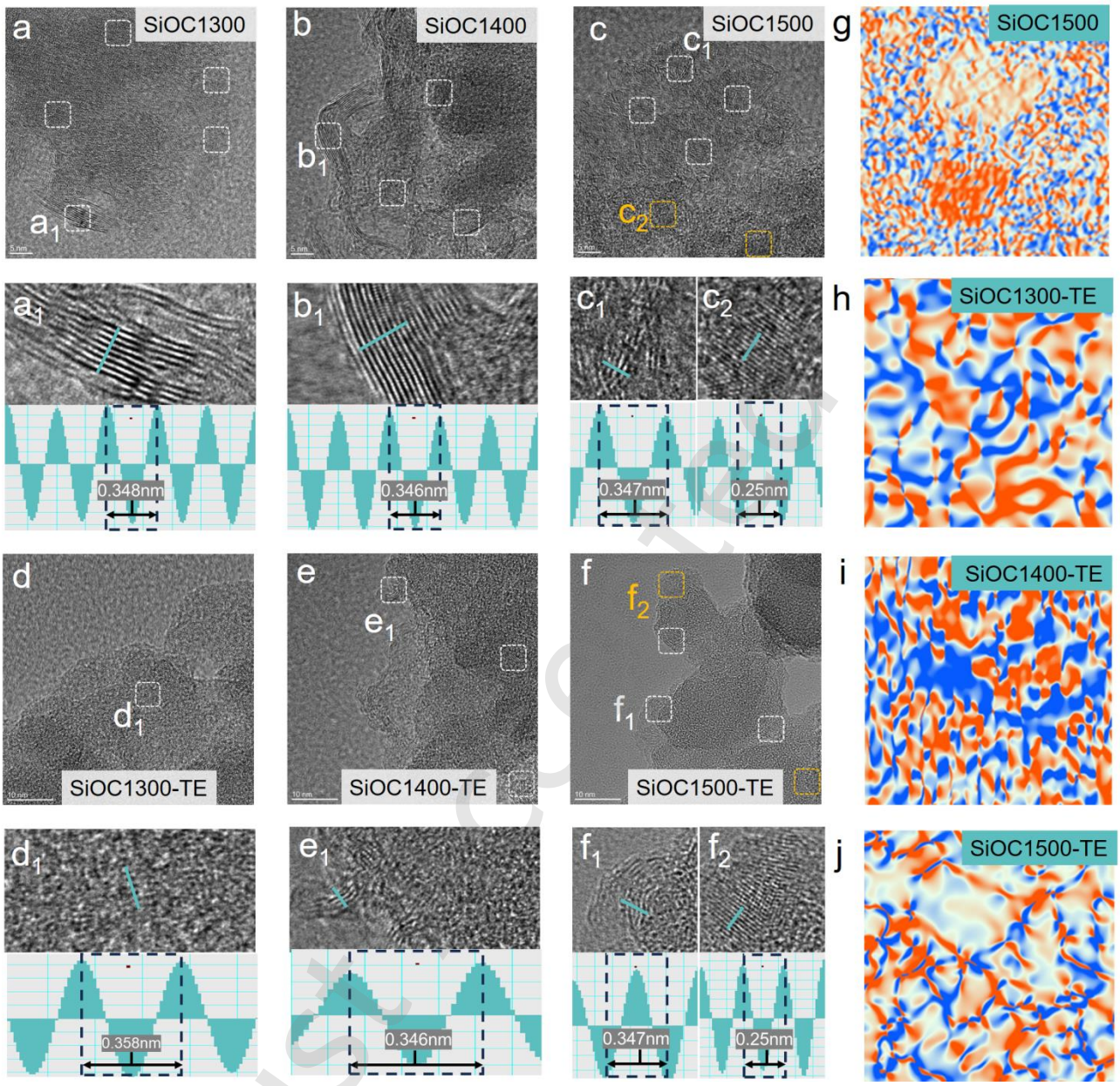


Fig. 3 Structural characterization of SiOC-derived ceramics pyrolyzed at 1300°C, 1400°C, and 1500°C, with and without thermal etching. (a–c) HRTEM images of SiOC1300, SiOC1400, and SiOC1500; (d–f) HRTEM images of SiOC1300-TE, SiOC1400-TE, and SiOC1500-TE. (a_1–c_2, d_1–f_2) zoom-in regions showing lattice fringes and corresponding schematic illustrations of fringe spacing. (g–j) 2D strain maps (GPA) of SiOC1500, SiOC1300-TE, SiOC1400-TE, and SiOC1500-TE.

Beyond localized lattice resolution, the macroscopic consequences of this nanodomain engineering on the dielectric environment are vividly visualized in the corresponding structural/strain field mapping images (Fig. 3g–j). These color maps graphically delineate the distribution of structural discontinuities across the micro-regions. It is evident that the high-temperature unetched SiOC1500 sample already

possesses intrinsic heterogeneity due to SiC precipitation (Fig. 3g). By comparison, the etched series exhibits profoundly intensified color contrast (Fig. 3h–j). This dramatically enhanced contrast indicates the prolific creation of dense, heterogeneous interfaces (SiC/residual carbon, carbon/amorphous matrix, and nanopore boundaries) following the partial carbon removal. In the context of electromagnetic wave absorption, these abundant heterogeneous interfaces act as massive localized capacitor networks. When subjected to an alternating electromagnetic field, they vigorously induce interfacial polarization and dipole polarization at defect sites. Consequently, this precise hetero-nanodomain engineering successfully suppresses excessive conduction loss to gain outstanding impedance matching, while concurrently amplifying polarization relaxation to ensure potent electromagnetic energy dissipation.

3.4 Microwave absorption performance of SiOCAMs

To comprehensively evaluate the electromagnetic wave attenuation capabilities of the designed composites, the reflection loss (RL) was calculated based on transmission line theory (Eq. (2) and Eq. (3))[41, 42]. Generally, an RL value inferior to –10 dB implies that 90% of the incident EM energy is effectively dissipated, defining the corresponding frequency range as the effective absorption bandwidth (EAB)[39, 43]. As depicted in the frequency-dependent RL curves and corresponding 2D contour mappings (Fig. 4a–h), the microwave absorption performance of the aerogel microspheres exhibits tunability governed by both the specific structural engineering and the matching thickness.

$$RL = 20\lg\left|\frac{Z_{in} - Z_0}{Z_{in} + Z_0}\right| \quad \text{Eq. (2)}$$

$$Z_{in} = Z_0\sqrt{\frac{\mu_r}{\varepsilon_r}}\tanh\left(j\frac{2\pi fd\sqrt{\mu_r\varepsilon_r}}{c}\right) \quad \text{Eq. (3)}$$

where Z_{in}, Z_0, c, and f denote the normalized input impedance of the absorber, impedance of air, velocity of light, and frequency of microwaves, respectively. Furthermore, ε_r, μ_r, and d represent the relative complex permittivity, relative complex permeability, and thickness of the absorber, respectively.

Just Accepted

The SiOC1200 sample exhibits a minimum reflection loss (RL_{min}) of –60.16 dB at 11.8 GHz (X band) and –54.06 dB at 14.28 GHz (Ku band), with a broad EAB of 7.66 GHz at a thickness of 2.7 mm (Fig. 4a and 4e). As the absorber thickness increases from 1.0 to 5.0 mm, the absorption peaks systematically shift toward lower frequencies, conforming strictly to the classic quarter-wavelength cancellation model. When evaluating the effect of higher carbothermal reduction temperatures (Fig. 4b and 4f), the SiOC1300 sample demonstrates an RL_{min} of –56.74 dB at 6.0 GHz (C band) and an EAB of 6.78 GHz at a reduced thickness of 2.2 mm. For the unetched SiOC1400 sample, while an RL_{min} of –48.68 dB is reached at 5.36 GHz, its EAB narrows significantly to 2.15 GHz. A further temperature increase to 1500 °C degrades the absorption capability, with the RL_{min} failing to reach –10 dB.

Hetero-nanodomain engineering via thermal etching effectively restores and enhances the microwave attenuation capacity. As illustrated in Fig. 4c and 4g, the etched SiOC1400-TE sample exhibits multiband absorption, recording RL_{min} values of –43.07 dB, –57.42 dB, –70.09 dB, and –61.42 dB at 13.16 GHz (Ku band), 11.16 GHz (X band), 9.04 GHz (X band), and 7.28 GHz (C band), respectively. Similarly, the SiOC1500-TE sample demonstrates a strong dual-band absorption profile, reaching an RL_{min} of –53.65 dB at 13.2 GHz and –57.87 dB at 5.36 GHz (Fig. 4d and 4h). This performance enhancement in the etched series indicates that the targeted removal of continuous amorphous carbon restructures the free-space impedance matching, thereby increasing incident microwave penetration. Concurrently, the retained heterogeneous interfaces act as effective dielectric loss centers.

Just Accepted

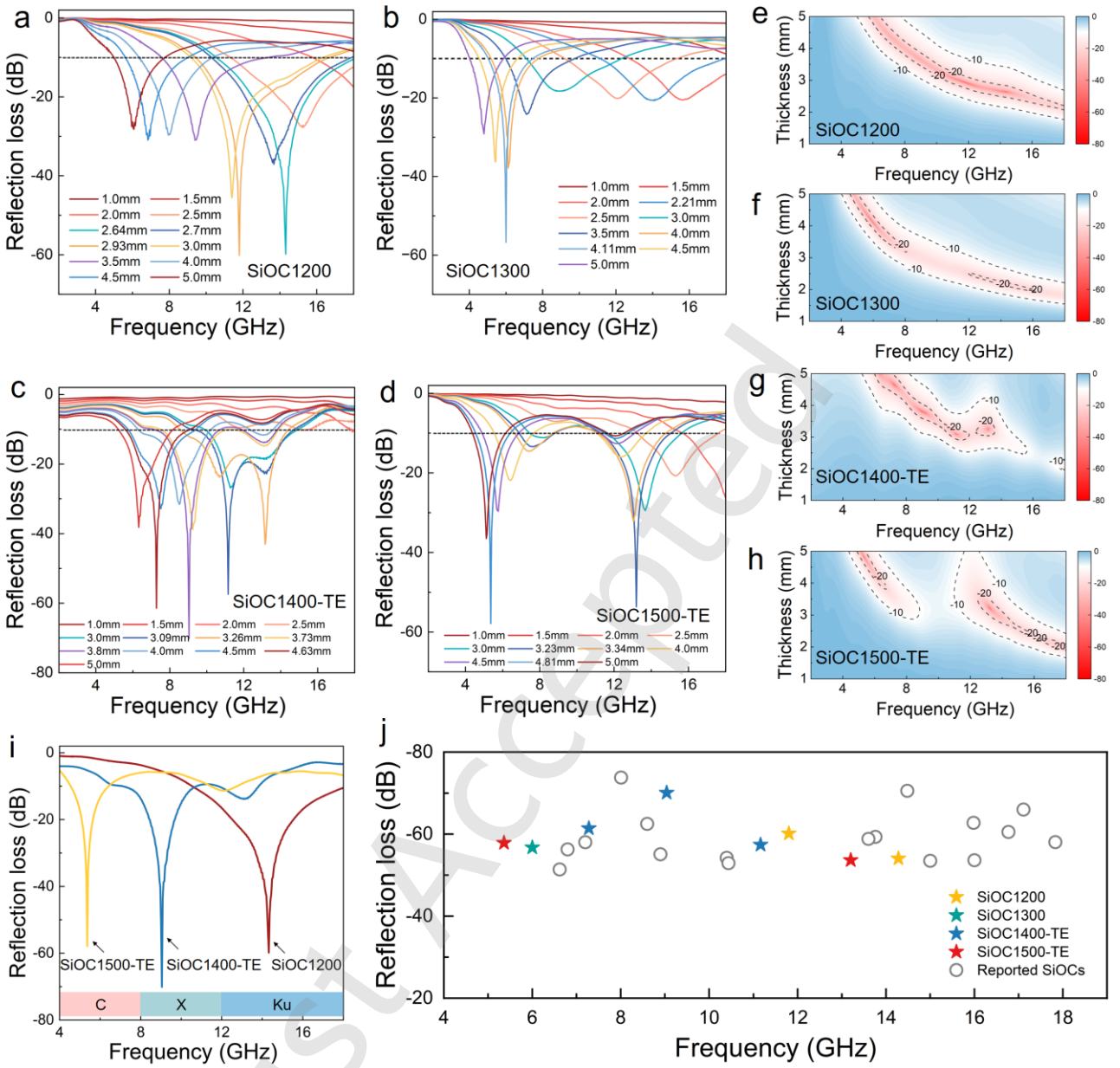


Fig. 4 Microwave absorption performance of the SiOC samples. Frequency-dependent RL curves at varied thicknesses for (a) SiOC1200, (b) SiOC1300, (c) SiOC1400-TE, and (d) SiOC1500-TE. Two-dimensional RL contour maps corresponding to (e) SiOC1200, (f) SiOC1300, (g) SiOC1400-TE, and (h) SiOC1500-TE, respectively. (i) Optimal RL curves demonstrating effective absorption in the C, X, and Ku bands for specific SiOC samples. (j) Comprehensive comparison of the minimum reflection loss performance between the materials prepared in this work and previously reported SiOC-based composites in the literature.

As depicted in Fig. 4i, the optimal absorption peaks of the tailored samples can be strategically shifted to encompass the C, X, and Ku bands. This breakthrough highlights a paradigm shift toward programmable electromagnetic wave absorption, demonstrating on-demand frequency tunability that far surpasses the confined absorption ranges typical of conventional counterparts. To comprehensively

Just Accepted

benchmark the engineered SiOC aerogel microspheres against contemporary SiOC-based composites, their overall capabilities—specifically RL_{min} across corresponding frequencies—are compared in Fig 4j. As clearly illustrated, individual literature reports (open circles) predominantly present static absorption profiles optimized for just one specific frequency band, fundamentally lacking a systemic strategy to tune absorption frequencies via structural adjustment. Conversely, the widespread distribution of diverse SiOC samples (solid stars) this work across the frequency axis provides direct evidence of true tunable absorption. Systematically tailoring the composition and structural domains via varying pyrolysis temperatures and etching processes effectively programs different samples to anchor their optimal absorption peaks at dynamically different target frequencies. This deliberate frequency assignation from the C band to the Ku band solidifies the advantage of SiOC series over the non-tunable nature of contemporary equivalents.

To unravel the underlying fundamental mechanisms responsible for the enhanced microwave absorption performance, the corresponding intrinsic dielectric parameters—namely, the real part (ε') and the imaginary part (ε'') of complex permittivity, along with the dielectric loss tangent ($\tan\delta_\varepsilon$)—were systematically evaluated across the 2–18 GHz range. As the composites are entirely non-magnetic, dielectric dissipation acts as the sole driver for electromagnetic wave attenuation. As observed in Fig. 5a–c and Fig. S8, for the unetched samples (SiOC1200 to SiOC1500), both the ε' and $\varepsilon''$of the complex permittivity undergo a dramatic upward shift with increasing pyrolysis temperature across 2–18 GHz. Specifically, SiOC1200 and SiOC1300 maintain relatively low and stable dielectric values, representing a state of weak dielectric loss. However, SiOC1500 displays a marked increase in permittivity alongside pronounced frequency dispersion. This elevation is predominantly driven by the accelerated graphitization of the free-carbon phase and the crystallization of SiC at higher temperatures, which collectively facilitate electron transport and dielectric loss. Following thermal etching, the dielectric behavior of SiOC1400-TE and SiOC1500-TE is drastically reshaped, characterized by the emergence of intense, distinct resonance peaks in both the ε'' and $\tan\delta_\varepsilon$ curves. These peaks signify

Just Accepted

that the etched porous structure and abundant hetero-interfaces facilitate additional dielectric mechanisms, notably interfacial polarization and dipole relaxation.

To quantitatively decouple the origins of this distinct dielectric behavior, the imaginary part of the permittivity was resolved into conduction loss (ε_c'') and polarization relaxation loss (ε_p'') contributions (Eq.(4)), based on the Debye relaxation theory[44-46] (Fig. 5d,e). The unetched samples exhibit dominant ε_c'' values at lower frequencies due to their highly interconnected graphitic/amorphous carbon networks. However, for the etched samples (SiOC1400-TE and SiOC1500-TE), the ε_c'' contribution experiences a precipitous drop (Fig. 5d). This affirms that the targeted oxidative etching truncates the over-percolated macroscopic carbon conductive routes. Concurrently, the ε_p'' emerges to completely dominate the overall imaginary permittivity for the etched series (Fig. 5e). These prominent polarization peaks are fundamentally rooted in the genesis of massive heterogeneous interfaces post-etching, which heavily accumulate space charges under an alternating electromagnetic field, triggering intense interfacial polarization[41, 45, 47].

$$\varepsilon'' = (\varepsilon_s - \varepsilon_\infty)\frac{2\pi f\tau}{1+(2\pi f\tau)^2\tau^2} + \frac{\sigma}{2\pi f\varepsilon_o} = \varepsilon_p'' + \varepsilon_c'' \quad \text{Eq. (4)}$$

This polarization-dominated attenuation landscape is further validated by the classical Cole-Cole plots (Fig. 5f). According to the Debye theory, each distinct semicircle represents an individual polarization relaxation process[48]. The unetched series exhibit protracted straight tails, indicative of a continuous conductive network. Conversely, the etched samples (particularly SiOC1400-TE and 1500-TE) exhibit multiple semicircles. These semicircles serve as definitive proof of multiscale polarization events, originating from dipole orientation at oxygenated/defect sites newly induced by etching, coupled with massive interfacial polarizations at the intricately engineered phase boundaries.

The microwave dissipation behavior is fundamentally governed by the impedance matching and the attenuation constant (α) as calculated using Eq. (5)[49, 50]. As displayed in Fig. S9, the pristine SiOC samples (SiOC1200 to SiOC1500) exhibit a monotonic increase in α with frequency, where higher

Just Accepted

annealing temperatures yield elevated attenuation values across the 2–18 GHz range, with SiOC1500 reaching the highest value exceeding 570. In contrast, the thermal-etched samples present altered attenuation profiles characterized by distinct resonance peaks: SiOC1500-TE displays a pronounced peak at ~10.5 GHz before stabilizing in the high-frequency region, whereas SiOC1400-TE and SiOC1300-TE exhibit peaks centered near 12.5 GHz and 12.0 GHz, respectively, maintaining overall moderate attenuation levels across the measured band.

$$\alpha = \frac{\sqrt{2}\pi f}{c}\sqrt{(\mu''\varepsilon'' - \mu'\varepsilon') + \sqrt{(\mu'\varepsilon'' + \mu''\varepsilon')^2 + (\mu''\varepsilon'' - \mu'\varepsilon')^2}} \quad \text{Eq. (5)}$$

Simultaneously, the 2D contour maps of the impedance matching across various thicknesses and frequencies illustrate the penetration behavior of incident electromagnetic waves (Fig. 5g–j), where regions approaching $|Z_{in}/Z_0| \approx 1.0$ indicate favorable matching conditions. For SiOC1200, a distinct $|Z_{in}/Z_0| \approx 1.0$ band extends from 4 GHz to 16 GHz (Fig. 5g). In contrast, the $|Z_{in}/Z_0| \approx 1.0$ region for SiOC1300 is confined to the low-frequency band (3–7 GHz) at larger thicknesses (Fig. 5h). After thermal etching, the matching profiles undergo reconfiguration: SiOC1400-TE displays a broad and continuous $|Z_{in}/Z_0| \approx 1.0$ domain distributed over the 6–16 GHz range within a thickness window of 1.5–4.5 mm (Fig. 5i), whereas SiOC1500-TE exhibits favorable matching regions concentrated in the low-to-mid frequency spectrum (Fig. 5j). As a result, the pristine samples exhibit effective single-band dissipation concentrated in targeted low or high frequencies, while the thermal-etched series achieves versatile multiband and broad-spectrum absorption performance across complementary operational bands.

.

Just Accepted

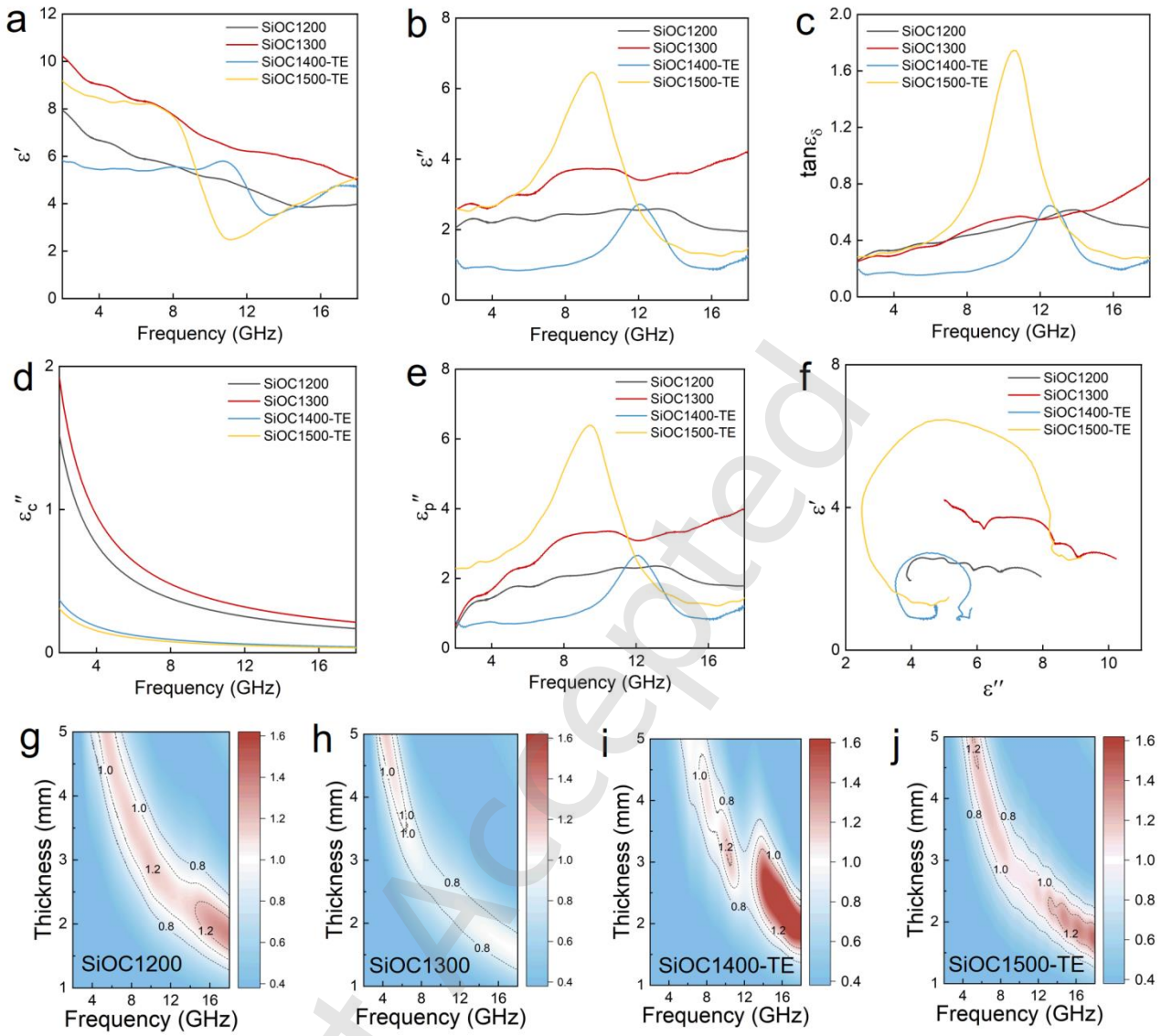


Fig. 5 Electromagnetic properties, dielectric loss mechanisms, and impedance matching of the prepared SiOC samples. Frequency dependence of the (a) real part (ε′) and (b) imaginary part (ε″) of complex permittivity. (c) Dielectric loss tangents (tanδ_ε). Calculated contributions of (d) conduction loss (ε_c'') and (e) polarization loss (ε_p''). (f) Cole-Cole plots showing the polarization relaxation processes. Two-dimensional contour maps of the impedance matching ratio ($|Z_{in}/Z_0|$) at different thicknesses for (g) SiOC1200, (h) SiOC1300, (i) SiOC1400-TE, and (j) SiOC1500-TE.

To comprehensively evaluate the radar stealth capabilities and validate the multi-band tunable design of the materials, CST Studio Suite 2025 was employed to simulate the spatial radar cross section (RCS) of PEC targets coated with the varying SiOCAMs. Fig. 6 and Fig. S10 presents the 3D scattering patterns and the corresponding 2D cross-sectional profiles for SiOC1200, SiOC1300, SiOC1400-TE, and SiOC1500-TE at their respective optimal matching thicknesses. The 3D radar scattering patterns visualize the spatial distribution of reflected energy[51]. Compare to bare metallic surfaces that exhibit

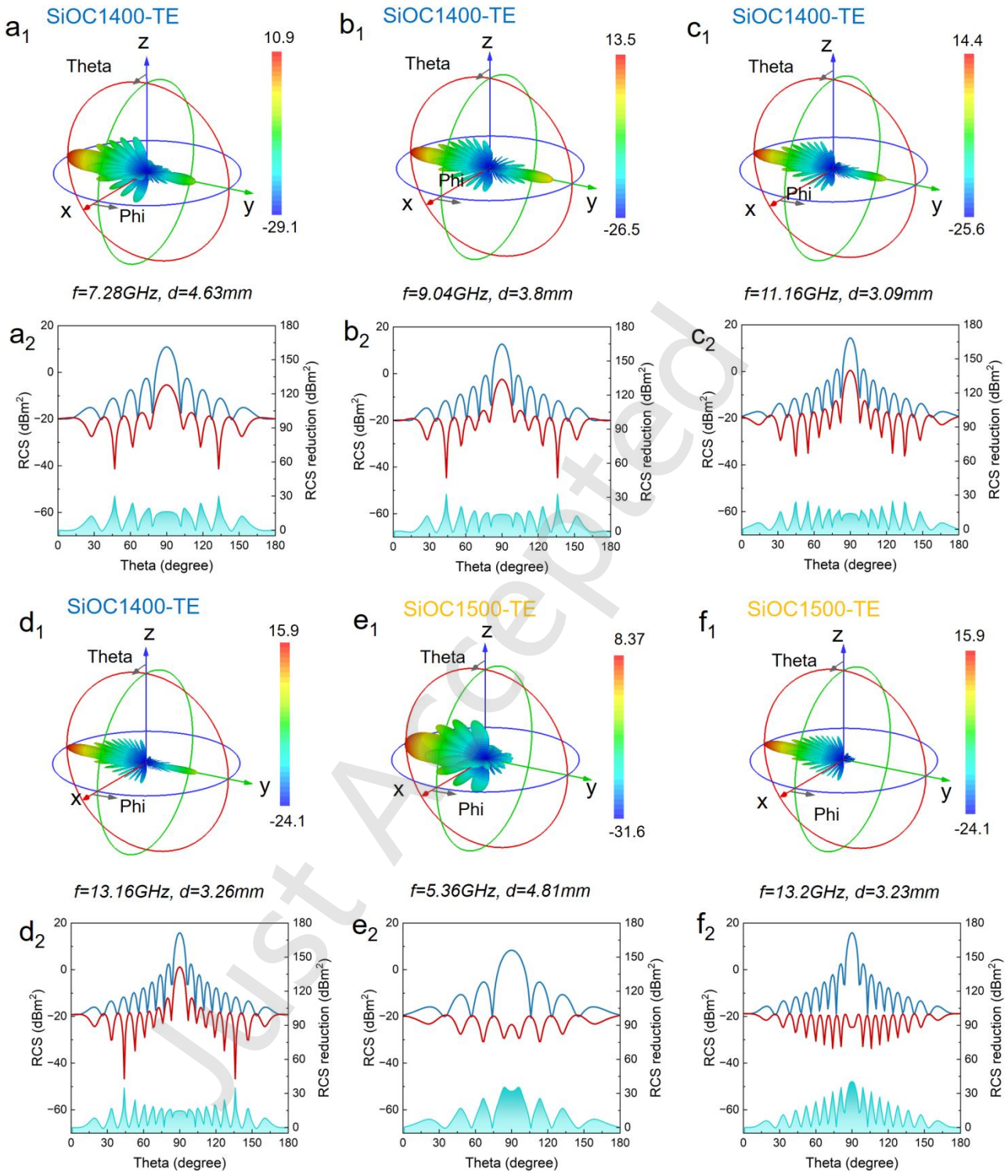
Just Accepted

intense forward-scattering main lobes (typically represented by red/yellow regions), the main lobes of all the aerogel-coated models show a significant color shift toward deep blue, confirming the substantial dissipation of incident electromagnetic waves by the macro-porous structures.

To quantify this spatial attenuation, transverse 2D angular scattering curves (θ from 0° to 180°) were plotted. Under identical incident fields, the angular reflection intensities of the absorber-coated targets are drastically suppressed across all angles compared to the pristine PEC. As summarized in the Table S, these configurations achieve remarkable RCS reduction values at the normal reflection angle (θ=90°), with a maximum reduction of 40.43 dBm^2 achieved by SiOC1500-TE at 13.2 GHz. The shaded cyan areas in the 2D profiles visually represent these substantial RCS reduction values, which consistently peak at the normal incidence angle across all samples.

Crucially, these results demonstrate that the dynamic frequency tunability is synergistically driven by internal hetero-nanodomain regulation and external geometric tailoring. On one hand, geometric modulation enables continuous tuning within a specific material: as demonstrated by the SiOC1400-TE series, simply adjusting the coating thickness (d) from 4.63 mm down to 3.26 mm shifts the optimal stealth frequency (f) from 7.28 GHz to 13.16 GHz. On the other hand, internal dielectric gene regulation unlocks completely new operational bands: by elevating the carbothermal reduction temperature and introducing post-oxidation thermal etching, the intrinsic multi-phase polarization and conduction behaviors are structurally reconfigured. This allows the targeted stealth bands to flexibly dip into the lower frequency ranges or cover the X and Ku bands on demand. These combined results fundamentally prove that the designed SiOCAMs break the narrow-band limitation of conventional absorbers, offering a highly versatile platform for multi-band radar stealth applications.

Just Accepted



Just Accepted

Fig. 6 Electromagnetic scattering simulations visualizing the radar stealth performance and frequency tunability of the absorbers. Panels (a–d) correspond to the SiOC1400-TE coated models, and panels (e, f) correspond to the SiOC1500-TE coated models at various specific target frequencies and coating thicknesses. The top rows (a_1–f_1) display the 3D spatial radar scattering patterns. The bottom rows (a_2–f_2) plot the corresponding quantitative 2D scattering profiles versus the elevation angle (θ), where the blue curves represent the bare PEC, the red curves represent the absorber-coated models, and the bottom shaded cyan regions indicate the absolute RCS reduction values.

To elucidate the macroscopic electromagnetic attenuation mechanisms of the bulk absorber, the electric field (E-field), current density, and power loss distributions of the stacked SiOC1200 (Fig. S11) and SiOC1400-TE (Fig. S12) aerogel microspheres were simulated at 5 GHz (C band), 10 GHz (X band), and 15 GHz (Ku band). As depicted in the E-field distributions (Fig. S13), electromagnetic waves effectively penetrate into the stacked architectures of both SiOC1200 (Fig. S13a_1–a_3) and SiOC1400-TE (Fig. S13b_1–b_3). Across 5 to 15 GHz, both samples display similar field distribution characteristics: the electric field is not entirely shielded at the front surfaces but penetrates into the inner array, accompanied by noticeable localized field concentrations at the inter-sphere contact necks and interstitial regions. These results demonstrate that the periodic packing geometry of the microspheres facilitates wave penetration and local field confinement[32, 38].

The corresponding current density and energy dissipation behaviors further reveal distinct frequency-dependent loss characteristics between the two samples (Fig. 7). For SiOC1200, both the current density (Fig. 7a_1–a_3) and power loss (Fig. 7b_1–b_3) exhibit frequency selectivity: at 5 GHz (C band), the power loss is almost negligible, but it intensifies as the frequency increases to 15 GHz (Ku band), where prominent high-loss hotspots cover the sphere surfaces (Fig. 7b_3). This demonstrates that the attenuation capability of SiOC1200 is biased toward the high-frequency regime while remaining inefficient at lower frequencies. In contrast, SiOC1400-TE maintains conduction and dissipation channels over the entire spectrum (Fig. 7c_1–c_3, d_1–d_3). Notably, at 5 GHz, SiOC1400-TE exhibits visible current paths and distinct energy dissipation hotspots at the contact nodes (Fig. 7d_1), generating a higher power loss than that of SiOC1200 in the C band. With increasing frequency to 10 and 15 GHz, high power loss is steadily preserved across the interconnected sphere boundaries (Fig. 7d_2, d_3). These simulation results confirm that, while SiOC1200 suffers from deficient attenuation at low frequencies despite its strong Ku-band response, the SiOC1400-TE achieves well-balanced dielectric loss across C, X, and Ku bands.

Just Accepted

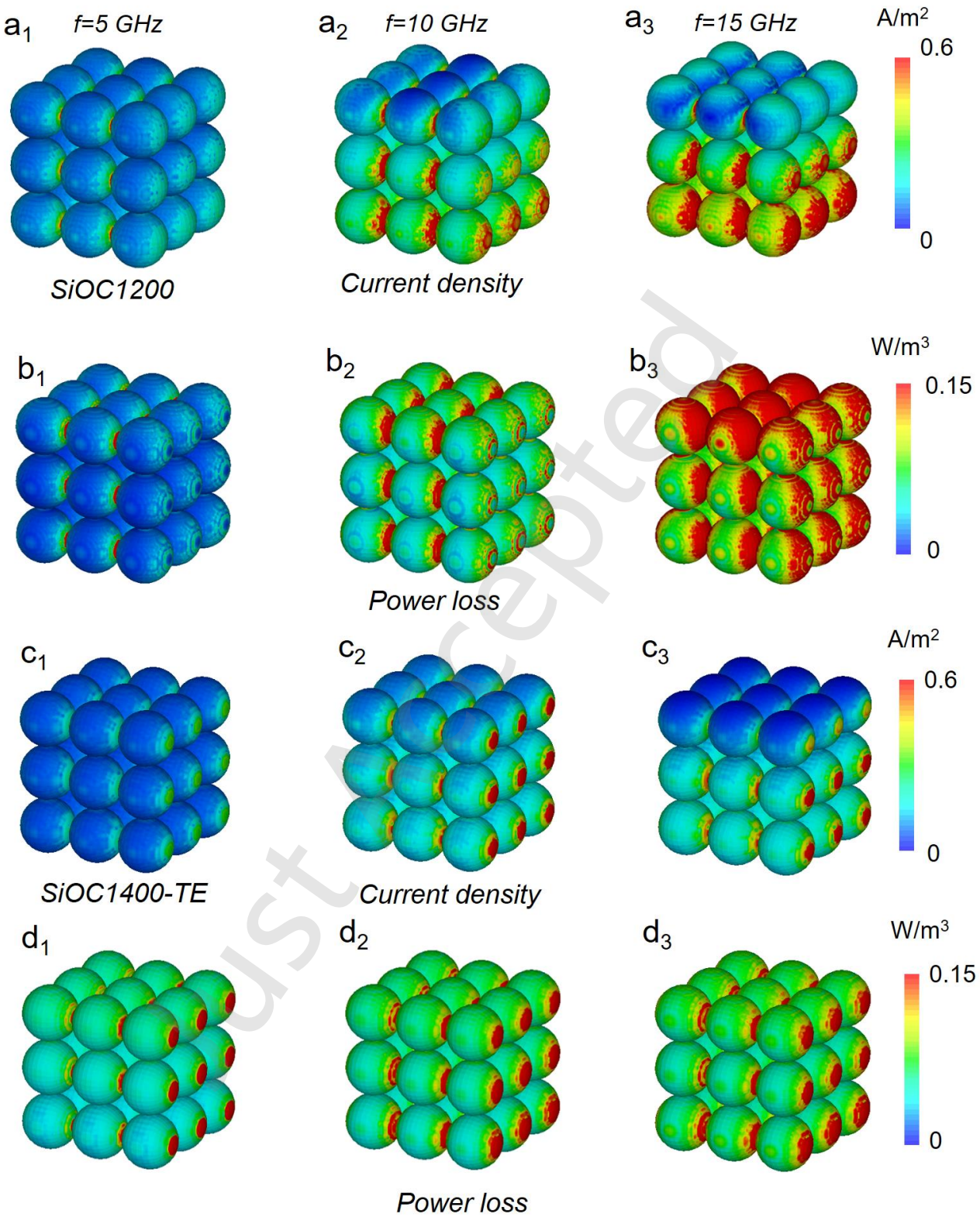


Fig. 7 Electromagnetic simulations illustrating the attenuation mechanisms in stacked aerogel microspheres: 3D spatial distributions of current density (a_1–a_3, c_1–c_3) and power loss density (b_1–b_3, d_1–d_3) for (a, b) SiOC1200 and (c, d) SiOC1400-TE at 5, 10, and 15 GHz.

Just Accepted

Crucially, this unique hierarchical morphology endows the composites with two synergistic structural advantages for microwave absorption (Fig. 8). First, the macroscopic interstitial voids formed by randomly packed microspheres construct a multi-scale air-solid dielectric environment, which effectively dilutes the effective permittivity and optimizes free-space impedance matching, thereby facilitating electromagnetic wave penetration with minimized surface reflection[31, 37]. Second, the highly porous intrinsic network within individual microspheres acts as an internal labyrinth, enhancing multiple scattering and extending the propagation paths of incident microwaves, thereby amplifying energy dissipation through prolonged wave-matter interaction. In essence, the hierarchical architecture constructs a physical foundation for wave entry and geometrical attenuation, whereas the subsequent nanoscale phase regulation, manifested through controlled heterointerface engineering, precisely dictates the dominant intrinsic loss mechanisms[52]. The interplay between conduction loss and polarization loss constitutes the dielectric gene of the material[53], enabling frequency-tunable absorption across C, X, and Ku bands through rational thermal treatment protocols. This structure–composition synergy exemplifies a systematic design methodology where the macroscopic architecture governs impedance matching and microscopic heterogeneity dictates dissipation efficiency, enabling lightweight, frequency-tunable electromagnetic wave absorption.

Just Accepted

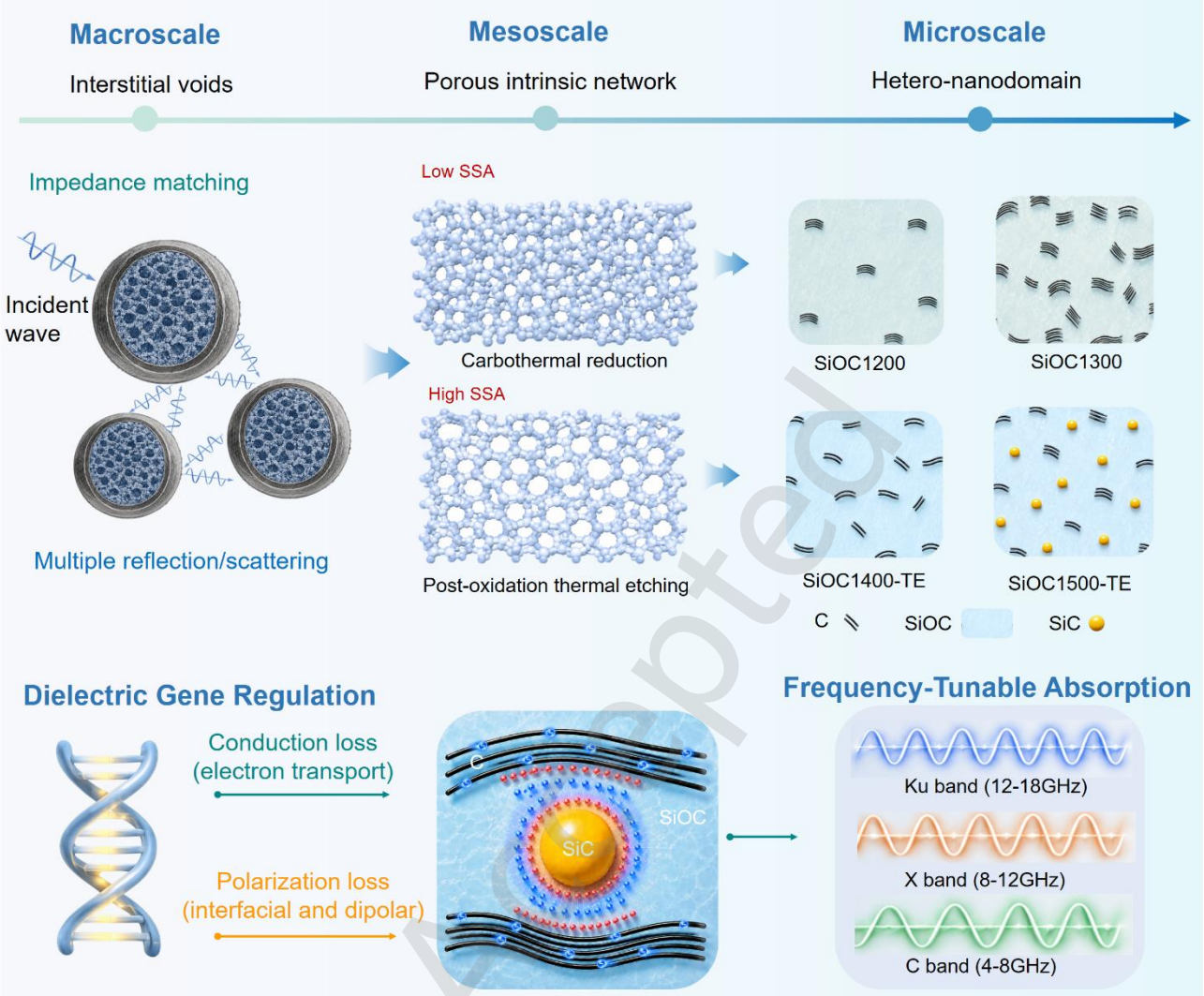


Fig. 8 Multi-scale structural design and synergistic microwave absorption mechanisms of hierarchical SiOC aerogel microspheres.

4 Conclusions

In conclusion, a multi-scale dielectric regulation strategy has been successfully demonstrated through the rational design of SiOCAMs. By integrating wet spinning, sol-gel processing, and precise thermal treatments, we bridged macroscopic structural architecture with microscopic hetero-nanodomain engineering. On a macroscopic level, the interstitial voids formed by the random packing of the aerogel microspheres create an ideal air-solid interface, significantly lowering the effective permittivity to ensure excellent impedance matching. Microscopically, the temperature-dependent evolution and post-oxidation tailoring of hetero-nanodomains (free carbon, SiC, and amorphous SiOC) effectively

Just Accepted

reconfigure the dielectric genes. This intrinsic regulation synergistically optimizes the conductive network and multi-relaxation polarization paths, maximizing the electromagnetic attenuation capability. As a result of this perfect macro-micro synergy, the proposed SiOCAMs exhibit state-of-the-art dynamically frequency-tunable absorption capabilities. They deliver minimum reflection losses of –57.87 dB, –70.09 dB, and –54.06 dB, spanning the C (5.36 GHz), X (9.04 GHz), and Ku (14.28 GHz) bands, respectively. This study elucidates the interplay between physical structural features and intrinsic dielectric parameters, offering a highly effective, generalized paradigm for designing lightweight ceramic absorbers for complex electromagnetic management.

Funding

The authors are grateful to the National Natural Science Foundation of China (52102361). Natural Science Foundation of Jiangsu Province (BK20211263). China Postdoctoral Science Foundation (2025T180037). Young Elite Scientists Sponsorship Program by Jiangsu Association for Science and Technology (JSTJ2023XH047),

Author contributions

Yong Kong: Methodology, Investigation, Formal analysis, Data curation, Writing-original draft, Validation. **Xiaoqian Zhang:** Investigation, Formal analysis, Data curation. **Jin Wei**: Investigation, Formal analysis, Data curation. **Yihang Yang:** Investigation, Visualization, Data curation. **Xiaodong Shen:** Supervision, Resources, Project administration. **Gaofeng Shao:** Conceptualization, Writing-review & editing, Supervision, Resources, Project administration, Funding acquisition.

Availability of data and materials

The data that support the findings of this study are available from the corresponding author upon reasonable request.

Just Accepted

Competing interests

The authors have no competing interests to declare that are relevant to the content of this article.

Data availability

The data that support the findings of this study are available from the corresponding author upon reasonable request.

Electronic Supplementary Material (ESM)

Electronic Supplementary Material: Supplementary material is available in the online version of this article).

References

[1] Zhang YY, Sun J, Wang YQ, *et al.* SiCN ceramics with controllable carbon nanomaterials for electromagnetic absorption performance. *J Am Ceram Soc* 2023, **106**: 4220–4232.

[2] Zhao WY, Shao G, Jiang MJ, *et al.* Ultralight polymer-derived ceramic aerogels with wide bandwidth and effective electromagnetic absorption properties. *J Eur Ceram Soc* 2017, **37**: 3973–3980.

[3] Song LM, Hu FY, Wang HG, *et al.* Advances in SiC aerogel materials for thermal insulation and electromagnetic wave absorption. *J Adv Ceram* 2026, **15**: 9221316.

[4] Wang XL, Fan XM, Hao HH, *et al.* Corrugated structure SiC_f/Si_3N_4 composite with high-temperature broadband microwave absorption through the regulation of high-temperature dielectric properties. *J Adv Ceram* 2026, **15**: 9221287.

[5] Zhang T, Bai BQ, Shao GF, *et al.* Hierarchically porous aerogels with heterogeneous nanodomains constructed from sub-1 nm nanowires for efficient microwave absorption. *Nano Res* 2026, **19**: 94908689.

[6] Gao BS, Yan YF, Zhang KL, *et al.* Ultralight Broadband Electromagnetic Wave Absorption Enabled by Interface-Engineered Two-layered Periodic Carbon Fiber Fabrics. *Adv Funct Mater* 2026, **36**: e32108.

Just Accepted

[7] Chen T, Yan YF, Liu SQ, *et al.* Lightweight and Flexible Fabric Assembled by ANF/GMWCNT Fibers for Broadband Electromagnetic Wave Absorption. *Adv Funct Mater* 2025, **36**: e28094.

[8] Zeng XJ, Deng XM, Yu ZJ, *et al.* Evolution of Fe Single Atom in SiOC Ceramic Fibers and Their High-Temperature and Ultrathin Electromagnetic Wave Absorption. *Adv Mater* 2026, **38**: e21533.

[9] Ren B, Jia YJ, Qi LH, *et al.* Broadband electromagnetic absorption up to 1473 K enabled by dielectric frequency-dispersion engineering in ceramic composites. *Nat Commun* 2025, **17**: 318.

[10] Zhou R, Wang YS, Liu ZY, *et al.* Digital Light Processing 3D-Printed Ceramic Metamaterials for Electromagnetic Wave Absorption. *Nano-Micro Lett* 2022, **14**: 122.

[11] Wen QB, Qu FM, Yu ZJ, *et al.* Si-based polymer-derived ceramics for energy conversion and storage. *J Adv Ceram* 2022, **11**: 197–246.

[12] Li W, Yu ZJ, Wen QB, *et al.* Ceramic-based electromagnetic wave absorbing materials and concepts towards lightweight, flexibility and thermal resistance. *Int Mater Rev* 2022, **68**: 487–520.

[13] Li DX, Jia DC, Yang ZH, *et al.* Principles, design, structure and properties of ceramics for microwave absorption or transmission at high-temperatures. *Int Mater Rev* 2022, **67**: 266–297.

[14] Du B, Liu YR, Chen Y, *et al.* Rational design of carbon-rich silicon oxycarbide nanospheres for high-performance microwave absorbers. *Carbon* 2023, **202**: 213–224.

[15] Qian JJ, Ma DD, Zhou XL, *et al.* Synthesis of SiOC@C ceramic nanospheres with tunable electromagnetic wave absorption performance. *J Adv Ceram* 2024, **13**: 1394–1408.

[16] Feng YR, Guo X, Elsayed H, *et al.* Enhanced electromagnetic microwave absorption properties of SiCN(Fe) ceramics produced by additive manufacturing via in-situ reaction of ferrocene. *Ceram Int* 2023, **49**: 25051–25062.

[17] Zhang BJ, Tong ZW, Wang X, *et al.* Zirconium-modified hierarchical porous SiC-based nanofibrous aerogel with efficient electromagnetic waves absorption and thermal insulation properties. *J Eur Ceram Soc* 2025, **45**: 116808.

[18] Niu M, Wang HJ, Su L, *et al.* Lightweight and resilient SiOC/SiC foam with efficient electromagnetic wave absorption and high-temperature stability. *J Am Ceram Soc* 2023, **106**: 3078–3088.

[19] Qian JJ, Du B, He C, *et al.* Multiscale SiCnw and carbon fiber reinforced SiOC ceramic with enhanced mechanical and microwave absorption properties. *J Am Ceram Soc* 2022, **105**: 3456–3468.

[20] Cao WQ, Zhang M, Cao MS. A Perspective of Tailoring Dielectric Genes for 2D Materials Toward Advanced Electromagnetic Functions. *Adv Funct Mater* 2024, **34**: 2410928.

[21] Yu GY, Shao GF, Xu RP, *et al.* Metal–Organic Framework-Manipulated Dielectric Genes Inside Silicon Carbonitride toward Tunable Electromagnetic Wave Absorption. *Small* 2023, **19**: 2304694.

Just Accepted

[22] Cheng JY, Chen QK, Wang HH, *et al.* Engineering Dielectric Genes in Debye Relaxation Model toward Frequency-Band-Reliant Electromagnetic Responses. *Adv Mater* 2026, **38**: e21471.

[23] Shao GF, Sun Y, Yu GY, *et al.* Enhanced low-frequency microwave absorption via polarization loss in nanodomain-rich SiCN. *J Am Ceram Soc* 2025, **108**: e20538.

[24] Xu FH, Yang YH, Kong Y, *et al.* Fe_3Si-encapsulated SiC aerogels enable low-frequency electromagnetic wave absorption with extreme-temperature resistance and thermal insulation. *Compos Part B Eng* 2026, **311**: 113204.

[25] Xu FH, Wei J, Yang YH, *et al.* In situ confinement of Co_2Si within SiC aerogels for low-frequency electromagnetic wave absorption. *Chem Eng J* 2026, **534**: 175230.

[26] Yang JC, Wen QB, Feng B, *et al.* Microstructural evolution and electromagnetic wave absorbing performance of single-source-precursor-synthesized SiCuCN-based ceramic nanocomposites. *J Adv Ceram* 2023, **12**: 1299–1316.

[27] Wang WC, Wang LY, Huang J, *et al.* Multi-heterointerface lightweight ceramics achieving temperature-insensitive dielectric properties for high-temperature electromagnetic wave effective absorption. *J Adv Ceram* 2025, **14**: 9221135.

[28] Song LM, Hu FY, Chen YQ, *et al.* Heterointerface-Engineered SiC@SiO_2@C Nanofibers for Simultaneous Microwave Absorption and Corrosion Resistance. *Adv Sci* 2025, **12**: e09071.

[29] Hao B, Zhang Y, Si HX, *et al.* Multiscale Design of Dielectric Composites for Enhanced Microwave Absorption Performance at Elevated Temperatures. *Adv Funct Mater* 2025, **35**: 2423897.

[30] Zhao YY, Song LM, Wang LN, *et al.* Biomass-derived anisotropic silicon carbide aerogels with orientation-dependent electromagnetic absorption and high-temperature insulation performance. *Defence Technol* 2026, **61**: 1–14.

[31] Shao GF, Xu RP, Chen Y, *et al.* Miniaturized Hard Carbon Nanofiber Aerogels: From Multiscale Electromagnetic Response Manipulation to Integrated Multifunctional Absorbers. *Adv Funct Mater* 2024, **34**: 2408252.

[32] Yang YH, Gu HY, Li YA, *et al.* Subwavelength functional-unit strategy based on magnetic-dielectric aerogel microspheres for broadband, wide-angle, and polarization-insensitive electromagnetic wave attenuation. *J Mater Sci Technol* 2027, **283**: 273–281.

[33] Yang DD, Dong S, Cui TY, *et al.* Multifunctional Carbon Fiber Reinforced C/SiOC Aerogel Composites for Efficient Electromagnetic Wave Absorption, Thermal Insulation, and Flame Retardancy. *Small* 2024, **20**: 2308145.

[34] Yang Q, Chen PA, Li XC, *et al.* Rational design of SiBCN ceramics with excellent attenuation to strong electromagnetic-wave-absorbing properties at low frequency. *Compos Part B Eng* 2024, **280**: 111486.

Just Accepted

[35] Yang DD, Dong S, Xin JQ, *et al.* Robust and thermostable C/SiOC composite aerogel for efficient microwave absorption, thermal insulation and flame retardancy. *Chem Eng J* 2023, **469**: 143851.

[36] Zhou Q, Zhang Y, Li Y, *et al.* Multi-scale GNS/SiC@SiBCN hybrid aerogels with tailorable electromagnetic wave absorption via hierarchical design. *Carbon* 2026, **246**: 120911.

[37] Li T, Li JT, Zhi DD, *et al.* Top-Level Electromagnetic Design of Multishell Resonant Cavity for Microspherical Microwave Structural Absorbers. *Small Struct* 2025, **6**: 2400666.

[38] Lin JP, Wang LC, Chu WQ, *et al.* Ultrabroadband Low-Frequency Microwave Absorption in Multiscale Aerogel-Metamaterial Hybrids. *Adv Funct Mater* 2026, **36**: e27401.

[39] Liu A, Zhang YL, Xu XS, *et al.* Multi-Field Synergy for Orchestrating Filler Angles in Polyimide Aerogels with Switchable Electromagnetic Interference Shielding. *Adv Mater* 2026, **38**: e73267.

[40] Song LM, Zhang F, Chen YQ, *et al.* Multifunctional SiC@SiO_2 Nanofiber Aerogel with Ultrabroadband Electromagnetic Wave Absorption. *Nano-Micro Lett* 2022, **14**: 152.

[41] Zhong X, Gu JW. Core-shell Co-C@CNT engineered to enable concurrent thermal conductivity and microwave absorption for Poly(4, 4′-dihydroxybiphenyl isophthalate). *Trans Mater Res* 2026, **2**: 100184.

[42] Yan YF, Lun AQ, Gao BS, *et al.* Advances in TMDs-Based Electromagnetic Wave Absorbers: From Structural Engineering to Multicomponent Synergy. *Nano-Micro Lett* 2027, **19**: 21.

[43] Qin GY, Liu YN, Yan YF, *et al.* Continuously Adjustable Impedance Gradient in Laminar Aerogels: Synergizing Matching and Multi-Position Attenuation for Broadband Absorption. *Adv Funct Mater* 2026, **36**: e19796.

[44] Zhang KL, Wang Z, Yan YF, *et al.* Dielectric–magnetic manipulation of reduced graphene oxide permittivity for enhanced electromagnetic wave absorption. *J Adv Ceram* 2024, **13**: 1974–1984.

[45] Yan YF, Cheng ZY, Chen T, *et al.* Rational high-entropy doping strategy via modular in situ/post solvothermal doping integration for microwave absorption. *J Adv Ceram* 2025, **14**: 9221168.

[46] Lin JP, Liu JR, Zhang KX, *et al.* Ambient-Pressure-Dried Aerogel Amplifies Interfacial Polarization Toward High-Efficiency Microwave Absorption. *Adv Funct Mater* 2026, **36**: e20336.

[47] Zhong X, He MK, Zhang CY, *et al.* Heterostructured BN@Co-C@C Endowing Polyester Composites Excellent Thermal Conductivity and Microwave Absorption at C Band. *Adv Funct Mater* 2024, **34**: 2313544.

[48] Chen YQ, Chen M, Lei H, *et al.* Microwave-assisted synthesis of high-performance TaC nanorods for enhanced electromagnetic wave absorption. *J Adv Ceram* 2025, **14**: 9221130.

[49] He MK, Zhong X, Lu XH, *et al.* Excellent Low-Frequency Microwave Absorption and High Thermal Conductivity in Polydimethylsiloxane Composites Endowed by Hydrangea-Like CoNi@BN Heterostructure Fillers. *Adv Mater* 2024, **36**: 2410186.

Just Accepted

[50] Huang J, Yu C, Liu YF, *et al.* Construction of hierarchical pores and polarization centers in PCN/MXene/ZnS@NC fibers for multiple-frequency and multifunctional electromagnetic wave absorption. *J Mater Sci Technol* 2027, **284**: 260–268.

[51] Huang B, Ye F, Deng JW, *et al.* Cross-scale structural engineering of MOF-derived Co_xNi_y@C nanorods with controllable electromagnetic response behavior for broadband electromagnetic wave absorption. *J Adv Ceram* 2026, **15**: 9221224.

[52] Song LM, Song C, Hu FY, *et al.* Janus Nanostructures Enabled by Confined Interfacial Engineering for Enhanced Electromagnetic Response. *Adv Sci* 2026, e77021.

[53] Huang GA, Zu DF, Jiang XW, *et al.* Phase evolution and broadband electromagnetic wave absorption mechanisms of electrospun polymer-derived SiC-based fibrous ceramic membranes. *J Adv Ceram* 2026, **15**: 9221349.

Just Accepted